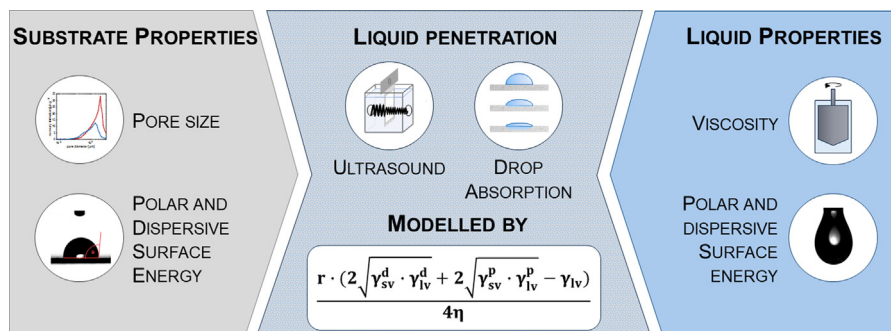# Modeling liquid penetration into porous materials based on substrate and liquid surface energies

Carina Waldner, Ulrich Hirn *

Institute of Bioproducts and Paper Technology, Graz University of Technology, Inffeldgasse 23, 8010 Graz, Austria
CD Laboratory for Fiber Swelling and Paper Performance, Inffeldgasse 23, 8010 Graz, Austria

GRAPHICAL ABSTRACT

ARTICLE INFO

ABSTRACT

Hypothesis: The widely used Lucas-Washburn (LW) equation depends on the contact angle as the driving force for liquid penetration. However, the contact angle depends on both, the liquid and the substrate. It would be desirable to predict the penetration into porous materials, without the requirement to measure the solid–liquid interaction. Here, we propose a novel modeling approach for liquid penetration from mutually independent substrate- and liquid properties. For this purpose, the contact angle in the LW-equation is replaced by polar and dispersive surface energies, utilizing the theories of Owens-Wendt-Rabel-Kaelble (OWRK), Wu, or van Oss, Good, Chaudhury (vOGC).
Experiments: The proposed modelling approach is validated exhaustively by measuring penetration speed for 96 substrate-liquid pairings and comparing the results to model predictions based on literature- and measured data.
Findings: Liquid absorption is predicted very well (R^2 = 0.8–0.9) with all three approaches, spanning a wide range of penetration speed, substrate- and liquid surface energy, viscosity, and pore size. The models for liquid penetration without measurement of solid–liquid interaction (contact angle) performed well. Modeling calculations are entirely relying on physical data of the solid and the liquid phase (surface energies, viscosity and pore size), which can be measured or retrieved from databases.

1. Introduction

Laminar pore flow is usually described by Darcy's law. Taking the capillary pressure as the driving force (Young-Laplace equation) and assuming circular pores one obtains the

---

* Corresponding author at: Institute of Bioproducts and Paper Technology, Graz University of Technology, Graz, Austria.
 E-mail address: ulrich.hirn@tugraz.at (U. Hirn).

Lucas-Washburn (LW) equation, which has been used for about a century [1,2]. It can be shown that Darcy flow and LW flow are interchangeable, boiling down to exactly the same equation just with different constants (see electronic supplementary information (ESI), section 7), hence in the context of this work they are equivalent. LW relates the penetration speed dh/dt (in m s^{-1}) to the liquid viscosity η (in Pa s), liquid surface tension γ (in N m^{-1}), pore radius r (in m), penetration depth h (in m), and the contact angle between liquid and substrate θ, Eq. (1).

$$\frac{dh}{dt} = \frac{r\gamma\cos\theta}{4\eta h} \tag{1}$$

Since then, numerous adaptations have been proposed, mostly to account for tortuosity and pore shapes other than cylindric pores [3–5], and for sticky layers [6] or slippage [7,8] at the capillary walls. A recent review on proposed extensions to the Lucas-Washburn equation has been given by Cai et al. [9]. All these approaches referenced in [9] have in common that the interaction between liquid and solid is described by the contact angle θ. In principle, contact angles can easily be determined by contacting the liquid with the substrate. However, for porous materials the contact angle in LW models can be challenging as the actually measured contact angle is heavily influenced by drop size, liquid absorption into the substrate pores and surface roughness (compare e.g. [10]). Finally, using the contact angle to describe liquid penetration has one major drawback. If the surface tension of the liquid or the surface energy of the substrate are changed, the effect on liquid penetration cannot be directly predicted without measuring the contact angle. This dependence on the contact angle makes Lucas-Washburn based modeling of liquid absorption in porous materials error prone and cumbersome. For scientific models as well as engineering applications – e.g. product development situations where liquid absorption is supposed to be tuned by finding optimal pairs of porous substrate and liquid – it would be preferable to use a model that does not rely on direct measurement of the solid–liquid interaction (i.e. contact angle) but on parameters that are independently describing properties of the porous substrate and the liquid.

1.1. Liquid penetration based on LW and substrate and liquid surface energies

On a smooth and homogeneous substrate, the contact angle is affected by the surface energy of the solid γ_{sv}, the surface tension of the liquid γ_{lv} and the interfacial tension between liquid and substrate γ_{sl} (all in N m^{-1}), as described by the Young equation [11]:

$$\cos\theta = \frac{\gamma_{sv} - \gamma_{sl}}{\gamma_{lv}} \tag{2}$$

The interfacial tension γ_{sl} and the solid surface energy γ_{sv} however, are hard to measure. The key modeling approach here is to replace the contact angle θ in the LW equation by the liquid and substrate surface energies which can be either measured or taken from the literature. Approaches commonly used to determine the solid surface energy comprise those of Owens, Wendt, Rabel and Kaelble (OWRK)[12–14], van Oss, Good, Chaudhury (vOGC) [15], Wu [16], and Neumann [17,18]. From an engineering perspective the OWRK approach is appealing due to its widespread application and will therefore be used as the principal example. In order to demonstrate that this surface-energy-based modeling approach is generally applicable, also the contact angle models of Wu and van Oss et al. are evaluated (methods and results are included in the ESI).

1.1.1. Liquid penetration based on LW and OWRK

The OWRK approach assumes that both, solid surface energy and liquid surface tension, can be split into a dispersive and a polar contribution, Eq. (3), and that only forces of the same type interact with each other. Thus, the solid–liquid interfacial tension can be described by Eq. (4).

$$\gamma = \gamma^d + \gamma^p \tag{3}$$

$$\gamma_{sl} = \gamma_{sv} + \gamma_{lv} - 2\sqrt{\gamma_s^d \cdot \gamma_l^d} - 2\sqrt{\gamma_s^p \cdot \gamma_l^p} \tag{4}$$

When combining Eq. (4) with the Young equation (2), the contact angle can be expressed as:

$$\cos\theta = \frac{2\sqrt{\gamma_s^d \cdot \gamma_l^d} + 2\sqrt{\gamma_s^p \cdot \gamma_l^p}}{\gamma_{lv}} - 1 \tag{5}$$

Replacing the contact angle in the Lucas-Washburn equation (1) by Eq. (5) results in a penetration equation with only independent substrate and liquid properties (LW-OWRK model):

$$\frac{dh}{dt} = \frac{r \cdot (2\sqrt{\gamma_s^d \cdot \gamma_l^d} + 2\sqrt{\gamma_s^p \cdot \gamma_l^p} - \gamma_{lv})}{4\eta h} \tag{6}$$

In the literature, a combination of the Lucas-Washburn and OWRK theory has been used to determine the surface energies of powders [19] and gas diffusion layers for proton exchange membrane fuel cells [20,21]. Thereby, the Lucas-Washburn equation was used to calculate the contact angle within the porous media via sorption experiments. From these calculated contact angles, substrate surface energies were then determined via the OWRK approach. Lavi and Marmur [22] have used a combination of Lucas-Washburn and OWRK equations theoretically to predict penetration speed maxima. However, a combination of Lucas-Washburn and OWRK has not yet been utilized for prediction of liquid penetration into porous materials.

1.1.2. Liquid penetration based on LW and Wu

Similarly, also other surface energy theories can be applied to derive a penetration equation that relies only on independent substrate and liquid properties. The surface energy model according to Wu [16] is also based on the assumption that interfacial energies can be split into a polar and dispersive contribution (Eq. (3)). However, for the polar and dispersive interactions, a harmonic mean is used instead of a geometric one. Thus, the solid–liquid interfacial tension can be described by Eq. (7):

$$\gamma_{sl} = \gamma_{sv} + \gamma_{lv} - \frac{4\gamma_s^d \cdot \gamma_l^d}{\gamma_s^d + \gamma_l^d} - \frac{4\gamma_s^p \cdot \gamma_l^p}{\gamma_s^p + \gamma_l^p} \tag{7}$$

This expression can again be combined with the Young equation (2) to get an expression for the contact angle:

$$\cos\theta = \frac{1}{\gamma_{lv}} \cdot \left(\frac{4\gamma_s^d \cdot \gamma_l^d}{\gamma_s^d + \gamma_l^d} + \frac{4\gamma_s^p \cdot \gamma_l^p}{\gamma_s^p + \gamma_l^p} \right) - 1 \tag{8}$$

The contact angle in the Lucas-Washburn equation (1) can then be replaced by Eq. (8) (LW-Wu model):

$$\frac{dh}{dt} = \frac{r \cdot \left(\frac{4\gamma_s^d \cdot \gamma_l^d}{\gamma_s^d + \gamma_l^d} + \frac{4\gamma_s^p \cdot \gamma_l^p}{\gamma_s^p + \gamma_l^p} - \gamma_{lv} \right)}{4\eta h} \tag{9}$$

1.1.3. Liquid penetration based on LW and vOGC

The surface tension approach of van Oss, Good and Chaudhury [15] is often also referred to as acid-base approach. Again, the interfacial tensions can be split into an apolar (Lifshitz-van der Waals, ^{LW}) and a polar fraction (Lewis acid-base, ^{AB}):

$$\gamma = \gamma^{LW} + \gamma^{AB} \tag{10}$$

However, it is argued that the polar γ^{AB} component is the result of electron acceptor (γ^+) and electron donor (γ^-) interactions that are not additive. Therefore, the (rearranged) Young equation according to van Oss et al. is expressed as:

$$\cos\theta = \frac{2\sqrt{\gamma_s^{LW} \cdot \gamma_l^{LW}} + 2\sqrt{\gamma_s^+ \cdot \gamma_l^-} + 2\sqrt{\gamma_s^- \cdot \gamma_l^+}}{\gamma_{lv}} - 1 \tag{11}$$

Substituting the contact angle in the Lucas-Washburn equation (1) using equation (11) gives the combined LW-vOGC model:

$$\frac{dh}{dt} = \frac{r \cdot (2\sqrt{\gamma_s^{LW} \cdot \gamma_l^{LW}} + 2\sqrt{\gamma_s^+ \cdot \gamma_l^-} + 2\sqrt{\gamma_s^- \cdot \gamma_l^+} - \gamma_{lv})}{4\eta h} \tag{12}$$

1.2. Aim of the work

It is the aim of this work to investigate the applicability of a modeling approach outlined above - LW flow in combination with different models for liquid and substrate surface energies (OWRK, Wu and vOGC) - for the prediction of liquid penetration speed into porous materials. The models are validated with a set of substrates and liquids spanning a wide range of liquid/substrate surface energies, viscosity and porosities. It will be shown that the models work for both, measured data and literature values.

2. Materials and methods

In order to validate this approach of combining the Lucas-Washburn equation with surface energy theories, liquid penetration measurements of a combination of liquids and porous paper substrates were performed. All relevant substrate and liquid parameters were varied systematically. Fig. 1 (a) gives an overview of the measurements used to characterize the liquid properties (viscosity, surface tension, surface tension components) and the substrate properties (pore size, surface energy components). The liquid penetration behavior was then modeled by either Eq. (6), Eq. (9) or Eq. (12), using different surface energy models as illustrated in Fig. 1 (b). Liquid penetration speed was measured with ultrasound and drop absorption measurements. To predict the measured penetration data, the substrate pore size was determined from mercury intrusion porosimetry and the substrate surface energy from contact angle measurements with pure standard liquids. The test liquids were characterized by their viscosity and surface tension. To determine polar and dispersive components of the liquid surface tension, interfacial tension measurements in a purely dispersive liquid were performed.

2.1. Liquids

Six liquids were designed to cover a range of viscosities and surface tensions (four corner and one center point plus pure water). They are mixtures of water (MilliQ), glycerol (AnalaR®NORMA-PUR® from VWR, 99.5 %), 1,2-hexanediol (Alfa Aesar from Thermo Fisher Scientific, 97 %), and a dye (Naphthol Blue Black, 100%) as shown in Table 1. A higher glycerol content leads to a higher viscosity, while 1,2-hexanediol decreases the surface tension. The resulting liquid properties in terms of surface tension and viscosity are shown in Fig. 2. Except for water, these liquids approximately cover the operating range for liquids that can be jetted in an inkjet printer [23].

Viscosity was measured with an Anton Paar MCR 100 device with a double-gap concentric cylinder system (DG 26.7) at a shear rate of 1000 s⁻¹. After pre-shearing of 5 min at 20 °C, temperature

was increased by intervals of 5 °C during the measurement. Since all other measurements were performed at ambient conditions of 23 °C and 50% humidity (ISO 187), the reported viscosity values were interpolated between 20 °C and 25 °C.

The surface tension was measured via pendant drops in air using a Dataphysics OCA200. Density values are reported in Table 1 and were used for the calculation of surface and interfacial tensions as well as Worthington numbers. Liquid density was measured with an oscillating u-tube method with a Mettler-Toledo DE40 instrument. The viscosity and density of water was taken from [24].

Using the OWRK theory, the polar and dispersive component of the surface tension γ_l^p and γ_l^d can be determined from measurements of the interfacial tension of the liquids in a purely dispersive liquid [25]. For that, Eq. (4) is applied to a liquid–liquid interface (indices indicate different liquids):

$$\gamma_{12} = \gamma_1 + \gamma_2 - 2\sqrt{\gamma_1^d \cdot \gamma_2^d} - 2\sqrt{\gamma_1^p \cdot \gamma_2^p} \tag{13}$$

If liquid one is a hydrocarbon, the polar part of the surface tension γ_l^p is equal to zero. Accordingly, using Eq. (13) and the assumption that the total surface tension is made up of a polar and a dispersive part (Eq. (3)), the dispersive part of the surface tension of liquid two γ_2^d can be calculated from Eq. (14) if the interfacial tension between the hydrocarbon and the studied liquid γ_{12}, as well as the surface tension of both liquids is measured.

$$\gamma_2^d = \frac{(\gamma_1 + \gamma_2 - \gamma_{12})^2}{4\gamma_1} \tag{14}$$

The polar part of the surface tension can then be calculated by again applying Eq. (3).

Interfacial tension of the test liquids was measured in *n*-hexane (from Merck KGaA, 99%) and *n*-heptane (ROTIPURAN® from Carl Roth, 99%), again using pendant drop measurements on a Dataphysics OCA200 instrument. A quartz-glass cuvette was used as container for the dispersive liquid in which drops of the liquid to be analyzed were formed. A shielding of copper wires was installed to prevent electrostatic charges from affecting the measurements. The surface tension of *n*-hexane was given as 18.43 mN m⁻¹ and that of *n*-heptane as 20.14 mN m⁻¹ in the Dataphysics database[1]. The measurement setup first was validated via measurements of pure standard liquids for which the results were validated by literature values (for further information please refer to the ESI, Figure S1).

Furthermore, the Worthington number *Wo* was used to estimate the accuracy of the pendant drop measurements as suggested by Berry et al. [26]. It is defined as:

$$Wo = \frac{\Delta\rho g V_d}{\pi\gamma D_n} \tag{15}$$

$\Delta\rho$ is the density difference between the two involved phases (in kg m⁻³), *g* the gravitational acceleration (in m s⁻²), V_d the drop volume (in m³), γ the interfacial or surface tension measured (in N m⁻¹) and D_n the needle diameter used (in m). Berry et al. [26] found good accuracy for Wo ≥ 0.6.

The drop volume of the measured drops, interfacial tensions and Worthington numbers can be found in the ESI. The diameter of the used needle was 1.83 mm. Worthington numbers for pendant drop measurements in this work ranged from 0.72 to 0.74 for surface tension measurements in air, from 0.62 to 0.72 for interfacial tension measurements in *n*-hexane and from 0.54 to 0.84 for measurements in *n*-heptane, indicating good accuracy. Only the measurements of TLC and TLH in *n*-heptane were below
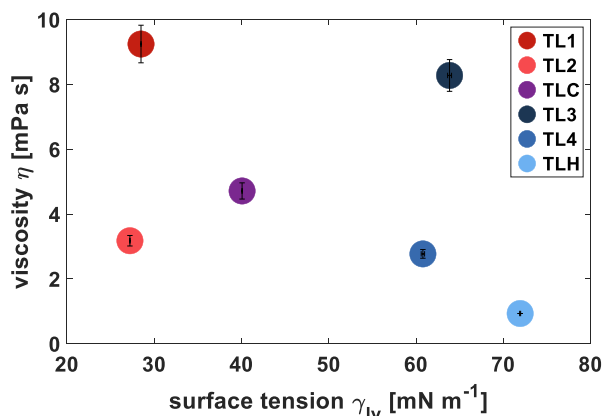

[1] Software SCA202 from Dataphysics, V.5.0.32, 2016.

(a)

(b)
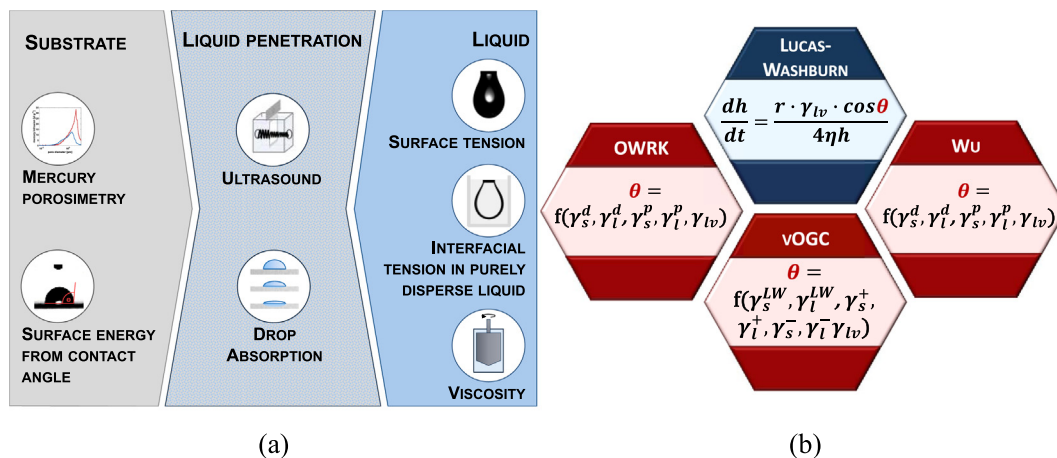
Fig. 1. (a) Overview of measurement methods used. Liquid penetration speed measured with ultrasound and drop absorption is predicted from substrate surface energy and pore size, as well as liquid viscosity and surface tension components. (b) Overview of modelling approaches used. OWRK, Wu and vOGC theory are used to replace the contact angle in the Lucas-Washburn equation with substrate surface energies and liquid surface tensions.

Table 1
Composition and properties of test liquids. Composition is given in mass fractions (m.f.). Surface tension components were calculated from interfacial tension measurements in *n*-hexane using the OWRK theory.

Test liquid	Water (mass fraction)	Glycerol (m.f.)	Hexane-diol (m.f.)	Dye (m.f.)	Density ρ [kg m^{-3}]	Viscosity η [mPa s]	Surface tension γ_{lv} [mN m^{-1}]	Dispersive surface tension γ_l^d [mN m^{-1}]	Polar surface tension γ_l^p [mN m^{-1}]
TL1	41.9	48.0	10.0	0.3	1117.2	9.248	28.5	27.4	1.1
TL2	64.9	25.0	10.0	0.3	1058.7	3.178	27.2	26.2	1.0
TL3	42.4	57.5	–	0.3	1146.2	8.278	63.8	35.5	28.3
TL4	64.8	35.0	0.1	0.3	1085.0	2.772	60.8	33.2	27.6
TLC	56.4	42.0	1.5	0.3	1111.7	4.714	40.1	25.5	14.6
TLH	100.0	–	–	–	997.5	0.933	71.9	26.2	45.7

Fig. 2. Test liquids with systematically varied surface tension and viscosity. Blue colors indicate a high surface tension, red colors a low surface tension. A darker color means a higher viscosity. Error bars indicate 95% confidence intervals. (For interpretation of the references to color in this figure legend, the reader is referred to the web version of this article.)
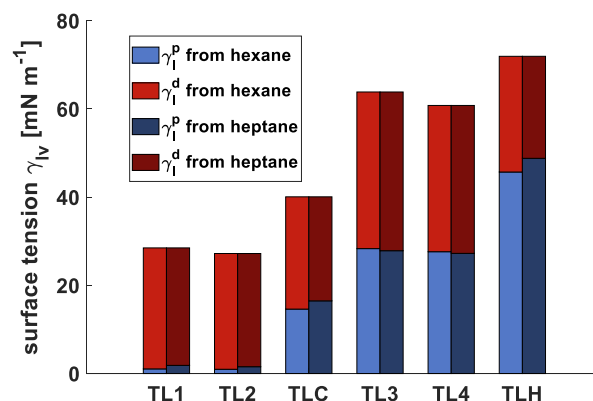
Fig. 3. Polar (γ_l^p, blue color) and dispersive (γ_l^d, red color) surface tension of the test liquids calculated from interfacial tension measurements in *n*-hexane (bright bars) and *n*-heptane (dark bars) according to OWRK theory. Both measurements gave similar results with minor deviations for TLC and TLH, indicating good reliability. (For interpretation of the references to color in this figure legend, the reader is referred to the web version of this article.)

0.6. Since the values of 0.54 respectively 0.56 were not much lower, reasonable accuracy is still expected.

Fig. 3 shows the polar and dispersive surface tension components of the test liquids calculated from interfacial tension measurements in *n*-hexane and *n*-heptane. Mostly, the polar part was affected by the addition of 1,2-hexanediol that was used to lower the surface tension. The results are similar for both measurements. The biggest deviations are found for the measurement of TLC and

TLH. This is in line with the Worthington number being below 0.6 for TLC and TLH in the *n*-heptane measurements. Therefore, the results of the *n*-hexane measurements seem to be slightly more trustworthy and will be used in all further evaluations.

Polar and dispersive liquid surface tension components according to Wu have been determined according to the same logic as described above for OWRK theory, while literature values for water were used for the vOGC approach. A detailed explanation is provided in the electronic supplementary information (ESI), section 3.

2.2. Substrates

To include the effect of substrate properties on liquid penetration, substrate porosity and surface energy were varied systematically as well. An industrially produced uncoated paper with a grammage of 89.6 g m^{-2} was the starting point. It was made up of cellulose pulp (mostly bleached eucalyptus kraft) and calcium carbonate fillers (scalenohedral, precipitated calcium carbonate, 21.25%). To modify its surface energy, the raw paper was treated via chemical vapor deposition. Hexamethyldisilazane (HMDS, from Carl Roth, 98 %) was used as hydrophobizing agent. Four levels were obtained by applying 0, 10, 20, or 40 mL of HMDS per 10 A4 sheets. The reaction conditions were 60 °C at 500 mbar for 24 h. Thereafter, the porosity and pore size of the papers was changed via calendering on a lab calender without calender roll heating at room temperature. Again, four levels were obtained by using calendering forces of 0, 15, 30, or 60 kN. For further details on the modification treatments please refer to [27]. By combining the four hydrophobicity levels with the four porosity levels, 16 different paper substrates were produced. Fig. 4 shows this 4 × 4 grid in a plot of Gurley air permeance (ISO 5636–5) vs. water contact angle (as measured for surface energy determination). Important properties of the papers are summarized in Table 2. Thickness and apparent density were determined according to DIN EN ISO 534.

To determine the substrate pore characteristics, Gurley measurements were used as a first indicator (compare Fig. 4). Since there were no significant differences between differently hydrophobized papers of the same calendering treatment, mercury intrusion porosimetry measurements were performed only for unhydrophobized papers using an Autopore IV 9500 instrument from Micromeritics Instrument Corp. Fig. 5 shows that calendering resulted in a reduction in pore size and intruded mercury volume, the effect being stronger for higher calendering intensities. For the validation of the combined LW-surface energy approaches, a pore radius is needed. The overall mean pore radius $\bar{r}$ was calculated as half of the sum of the mean pore diameter $\bar{d}_i$ in each size class i of the pore size distribution multiplied with each class's relative intruded mercury volume $\Delta Hg_i / \sum \Delta Hg_i$ (Eq. (16), results in Table 2).

$$\bar{r} = \frac{1}{2} \cdot \sum_{i=1}^{n} \bar{d}_i \cdot \frac{\Delta Hg_i}{\sum_{i=1}^{n} \Delta Hg_i} \tag{16}$$

To determine the surface energy components of the papers according to the OWRK approach, contact angles were measured with 2 μL drops of deionized water, ethylene glycol (from Carl Roth, 99%) and diiodomethane (ReagentPlus® from Sigma Aldrich, 99%) on all papers with a Dataphysics OCA200 instrument. The contact angle was evaluated as soon after drop deposition as possible. Some waiting time was necessary for the drop to be reasonably stable. By measuring the contact angle as early as possible, the impact of liquid penetration is minimized. The best compromise between drop stability and penetration differed for the liquids. Ethylene glycol contact angles were measured after 15 ms, diiodomethane contact angles after 50 ms. The substrates differed most in terms of water contact angles. Therefore, two evaluation times had to be chosen for the water measurements. For hydrophobized papers, the drops needed more time to stabilize and thus the contact angle was evaluated after 50 ms. For hydrophilic papers, on the other hand, water penetrated quickly and therefore the contact angles were determined already after 20 ms.

From the measured contact angles, the substrate surface energy components can be calculated by rearranging Eq. (5) to:
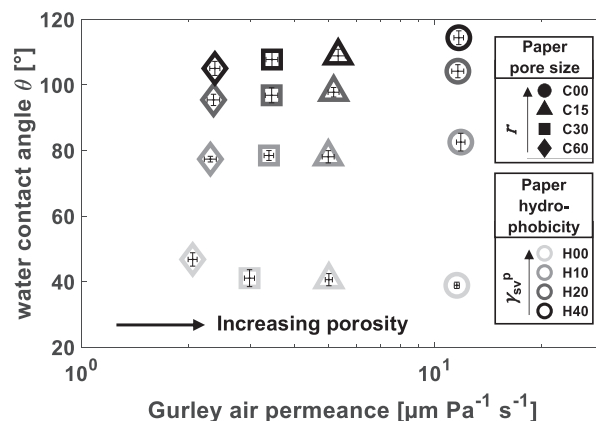

Fig. 4. Gurley air permeance and water contact angles used for surface energy calculation of the paper substrates. Shape of the marker indicates the pore size of the substrate and marker edge gray level the hydrophobicity, a darker gray being more hydrophobic. Error bars indicate 95% confidence intervals.

$$\frac{\gamma_{lv}(1+\cos\theta)}{2\sqrt{\gamma_l^d}} = \sqrt{\gamma_s^d} + \sqrt{\gamma_s^p} \cdot \sqrt{\frac{\gamma_l^p}{\gamma_l^d}} \tag{17}$$

Using the measured contact angle data together with literature values for the liquid surface tension components (taken from Dataphysics database[1]) a graph of $\sqrt{\frac{\gamma_l^p}{\gamma_l^d}}$ versus $\frac{\gamma_{lv}(1+\cos\theta)}{2\sqrt{\gamma_l^d}}$ can be created. A line is fitted to the three data points corresponding to the three measurement liquids. The dispersive component of the surface energy can then be determined as the square of the y-axis intercept. The polar component corresponds to the square of the slope. For some of the more hydrophobic papers, the slope of the fitted line was negative. In those cases, a slope of zero was assumed and a horizontal line was fitted instead. The calculated surface energy components of the papers are reported in Table 2. The hydrophobization treatment dramatically changed the polar component of the surface energy, while the calendering had only a minor effect on the dispersive component of medium to strongly hydrophobized papers.
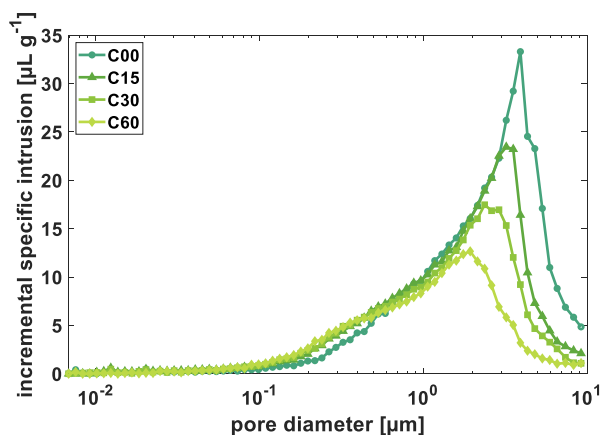
Polar and dispersive surface energy components of the substrates according to Wu and vOGC have been determined using an equivalent approach like described above for OWRK. The procedures are in detail explained in the electronic supplementary information (ESI), section 4.

2.3. Liquid penetration measurements

Liquid penetration speed was measured for all possible – i.e. 96 – substrate-liquid combinations with two methods. The first method is based on contact angle measurements which were performed with a Fibro DAT 1100 dynamic contact angle instrument using a drop size of 3.5 μL. The Fibro DAT was chosen for the absorption measurements because of its drop deposition method (deposition via a fast motion of the capillary) which allowed for a constant deposition procedure for all substrate-liquid pairings. 12 drops were measured per test point until they were absorbed or a maximum measurement time of 18 s was reached. Contact angle, drop volume, base diameter and drop height were recorded over time and outliers in terms of initial contact angle and/or drop volume were removed. Fig. 6 shows a sequence of images of a drop being absorbed into a paper substrate as recorded in the drop absorption measurements. Using the first and the last detected volume (V_{start} and V_{end} in μL) and the time interval passed (in s), an absorption rate in μL s^{-1} can be calculated. This absorption rate

Table 2
Properties of the paper substrates. Reported errors are 95% confidence intervals.

Paper	Thickness [µm]	Apparent density [g cm^{-3}]	Gurley air permeance [µm Pa^{-1} s^{-1}]	Mean pore diameter [µm]	Dispersive surface energy γ_s^d [mN m^{-1}]	Polar surface energy γ_s^p [mN m^{-1}]
C00_H00	132.4 ± 1.9	0.68	11.5 ± 0.2	2.80	20.3	25.3
C00_H10	134.3 ± 2.5	0.67	11.9 ± 0.3	2.80	37.8	1.1
C00_H20	132.4 ± 1.7	0.68	11.6 ± 0.5	2.80	33.6	0.0
C00_H40	132.0 ± 2.8	0.68	11.7 ± 0.4	2.80	23.6	0.0
C15_H00	100.0 ± 1.2	0.90	5.0 ± 0.1	2.16	21.8	23.5
C15_H10	99.1 ± 2.0	0.91	5.0 ± 0.2	2.16	36.1	2.5
C15_H20	100.8 ± 1.9	0.89	5.2 ± 0.2	2.16	38.3	0.0
C15_H40	99.9 ± 1.9	0.90	5.3 ± 0.3	2.16	32.0	0.0
C30_H00	94.9 ± 2.6	0.94	3.0 ± 0.1	1.89	22.2	23.7
C30_H10	95.8 ± 3.1	0.93	3.4 ± 0.1	1.89	36.4	2.4
C30_H20	94.8 ± 1.8	0.94	3.5 ± 0.1	1.89	39.8	0.0
C30_H40	94.6 ± 1.7	0.94	3.5 ± 0.1	1.89	32.2	0.0
C60_H00	92.3 ± 2.1	0.97	2.1 ± 0.1	1.51	25.1	19.5
C60_H10	91.8 ± 1.7	0.97	2.3 ± 0.1	1.51	34.1	3.2
C60_H20	91.1 ± 2.7	0.98	2.4 ± 0.1	1.51	41.0	0.0
C60_H40	92.2 ± 1.5	0.97	2.4 ± 0.1	1.51	34.1	0.0

Fig. 5. Pore size distributions from mercury intrusion porosimetry for the four calendering intensities used. Calendering reduced both pore size and intruded volume. Numbers precedented by "C" indicate the calendaring force used (in kN).
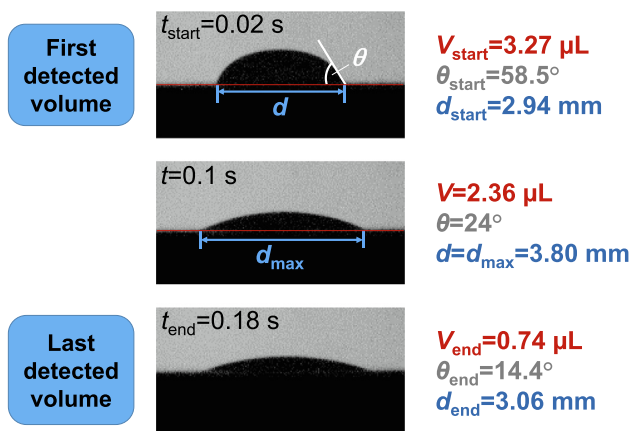
Fig. 6. Sequence of images of a drop on a paper substrate as recorded in the drop absorption measurement. The first and the last detected drop volume V_{start}, V_{end}, as well as the maximum detected base diameter d_{max} are used to calculate the drop absorption speed according to Eq. (18).

is further averaged over the area covered by the drop which was approximated from the maximum detected base diameter d_{max} (in mm). Accordingly, the drop absorption speed in m s^{-1} is defined by Eq. (18). Drop absorption speed was calculated for each drop

and then averaged for the 12 drops measured. Volume reduction due to evaporation was neglected as measurements on a non-absorbing substrate did not reveal any significant volume loss (compare section 5.1 Figure S6 in the ESI).

$$drop\ absorption\ speed = \frac{\Delta V}{\Delta t \cdot A}$$
$$= \frac{(V_{start} - V_{end}) \cdot 4}{(t_{end} - t_{start}) \cdot \pi \cdot d_{max}^2} \cdot 10^{-3} \qquad (18)$$

In addition to that, penetration speed was determined with ultrasonic liquid penetration measurements using a Penetration Dynamics Analyser 2.0 from emtec Electronic GmbH, Leipzig, Germany. Thereby, a sample of 5 × 7 cm is fixed onto a sample holder with two-sided adhesive tape and then rapidly immersed into a chamber filled with the test liquid. An ultrasound signal with a frequency of 2 MHz passes through a measurement area with 35 mm diameter and the transmission over time is recorded (compare Fig. 7 (a)). In case of capillary penetration, the transmitted signal decreases over time probably due to air bubbles being formed and entrapped during the continuing absorption which scatter the signal. Liquid penetration speed can thus be related to the speed of the signal decrease. Fig. 7 (b) shows typical ultrasound curves of differently hydrophobized papers in contact with water. More hydrophobic papers (darker line color) show a slower decrease of the signal intensity and thus penetration speed. For further information on the interpretation of ultrasonic liquid penetration measurements please refer to [28].

The ultrasonic liquid penetration speed *ULP* was calculated according to Eq. (19). The time until the signal decreased to 50 percent t_{50} was used as a reference. Dividing the intensity decrease in percent by the time interval passed gives a penetration speed in % s^{-1}. In case the signal did not decrease to 50 percent within the measurement time of 30 s, the last measured intensity and Eq. (20) were used instead. Four measurements were performed and averaged for each test point. For the three lighter blue curves in Fig. 7 (b) (papers with zero to medium hydrophobicity), *ULP* was calculated with Eq. (19). The dark blue curve represents a measurement of the strongly hydrophobized, uncalendered paper with water. In this case, the signal intensity never reached 50 percent and Eq. (20) was used accordingly.

$$ULP = \frac{\Delta I}{\Delta t} = \frac{100 - 50}{t_{50} - t_{start}} \qquad (19)$$

$$ULP = \frac{\Delta I}{\Delta t} = \frac{100 - I_{end}}{t_{end} - t_{start}} \qquad (20)$$
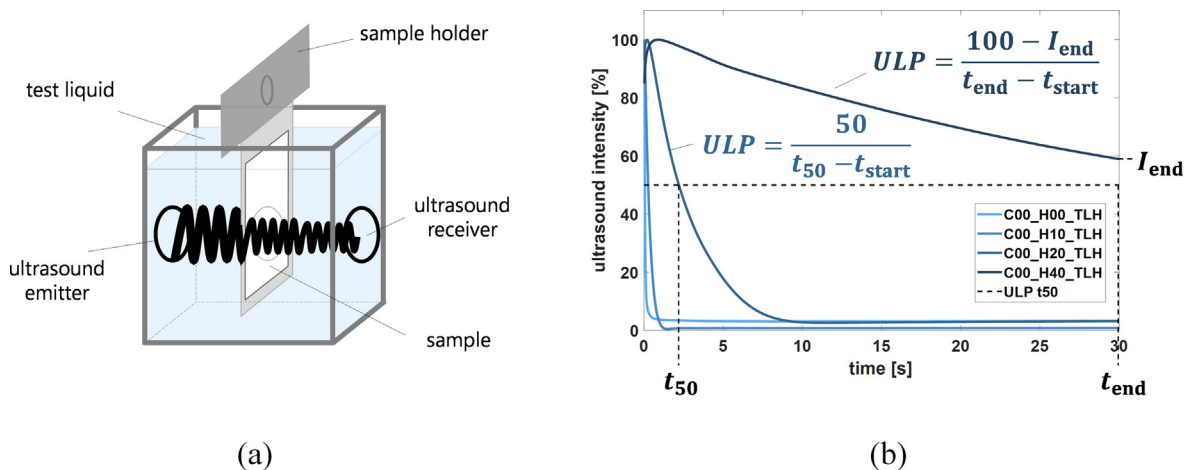
Fig. 7. (a) ULP measurement principle. The sample is immersed into a chamber filled with the test liquid and the transmitted ultrasound signal is recorded over time. (b) Example of recorded ultrasound curves. Penetration speed is indicated by the decrease of the ultrasound signal and calculated as percentage change over time. [27].

For more information on the liquid penetration measurement methods, their reliability and preferred operating windows please refer to [27]. As shown there, drop absorption speed could not be reliably determined from contact angle measurements if wetting was strong. Therefore, strong wetting substrate-liquid combinations (last measured contact angle smaller 18° and/or predicted contact angle of 0°) were eliminated from the evaluation with drop absorption measurements.

3. Results and discussion

The usage of surface energy models with liquid mixtures has been viewed critically because of concerns over preferential adsorption of one component [29,30], although binary mixtures have been used successfully for the calculation of surface energies with the OWRK approach [31,32] and the usage of liquid mixtures has even been recommended to improve the precision of surface energy estimations [31]. To ensure that the discussed surface energy theories can be applied to the liquid mixtures used, we will first evaluate if each theory can predict the wetting behavior of a liquid-substrate pairing before applying the combined LW-surface energy models for the prediction of liquid penetration speed.

### 3.1. Performance of LW-OWRK model

Fig. 8 compares contact angles predicted from surface energies with the OWRK method using Eq. (5) with the contact angles of the liquid mixtures on the paper substrates measured with the Fibro DAT at different evaluation times. In the first graph after 20 ms there is a rather large degree of scattering. The measured values are also higher than the predicted contact angle values. This is especially true for liquids with a higher viscosity (darker colors). The reason for that is that the drops did not have enough time to fully spread and spreading is slower if the viscosity is higher.

Evaluating the contact angles after 60 ms leads to a much better correlation between predicted and measured contact angles, although the measured contact angles still are somewhat higher than the predicted ones. This is especially true for substrate-liquid combinations for which a contact angle of 0° is predicted. Allowing some more time for spreading, after 100 ms the predicted contact angles are as high as the measured ones if the 0° data points are neglected (as indicated by the solid red fitted line overlapping with the 45° line). Also, a high R² of 0.88 is reached. Appar-

ently, the substrate-liquid pairings for which full spreading is predicted from the model do not follow the same trend. Even after 100 ms, the measured contact angles are still much higher than 0°. An explanation for that could be that the measured contact angle certainly is not the equilibrium contact angle and it would take longer to approach a contact angle of 0°. However, there are two mechanisms inhibiting drop spreading to full equilibrium. First, spreading stops in a metastable state if all kinetic energy is dissipated due to friction at the moving contact line which is caused by viscosity, roughness etc. [33]. Furthermore, absorption of these drops is particularly fast, taking place before full spreading is achieved. Thus, due to fast absorption, friction, and surface roughness, drops that would permit full spreading on smooth and non-absorbing surfaces never reach equilibrium and exhibit a considerably higher contact angle than predicted by the surface energies.

If the contact angles are evaluated at later times, the influence of absorption increases. All of the substrate-liquid pairings with a predicted contact angle of 0° could not be detected after 1063 ms either because they were absorbed or too flat for detection. For the remaining data points, the absorption impact results in lower measured contact angles compared to the predicted ones due to contact line pinning (graph after 1063 ms). That incomplete spreading is the reason for the deviations at early evaluation times and absorption is the reason for deviations at later times, is also shown by the fact that data points with unfavorable wetting conditions (contact angle > 90°) show no such time dependency. For these substrate-liquid pairings, drops neither spread nor penetrate.

Since the OWRK approach was successful in predicting the wetting behavior of the substrate-liquid pairings, it can now be combined with the Lucas-Washburn equation to predict penetration speed. Fig. 9 shows the results for the measured drop absorption speeds. Data points with strong wetting indicated by a predicted contact angle of 0° and/or a low contact angle at the end of the measurement (θ_{end} <=18°) were removed. The drop absorption measurement is not reliable in those cases because the contact angle instrument cannot deliver a reliable drop volume value for such low-height, wide spread drops, as described in [27]. In Fig. 9 (a), the drop absorption speeds can be predicted reasonably well (R² = 0.82) with the combined LW-OWRK model. The trends are captured also in the low absorbing region. However, the fit in Fig. 9 (a) is dominated by extreme values. Therefore, it is useful to look at a double-logarithmic chart as well. Fig. 9 (b) shows that penetration speed trends can be predicted over a wide range of penetration speeds with the combined LW-OWRK model. In the logarithmic chart, a similar R² of 0.83 is reached.
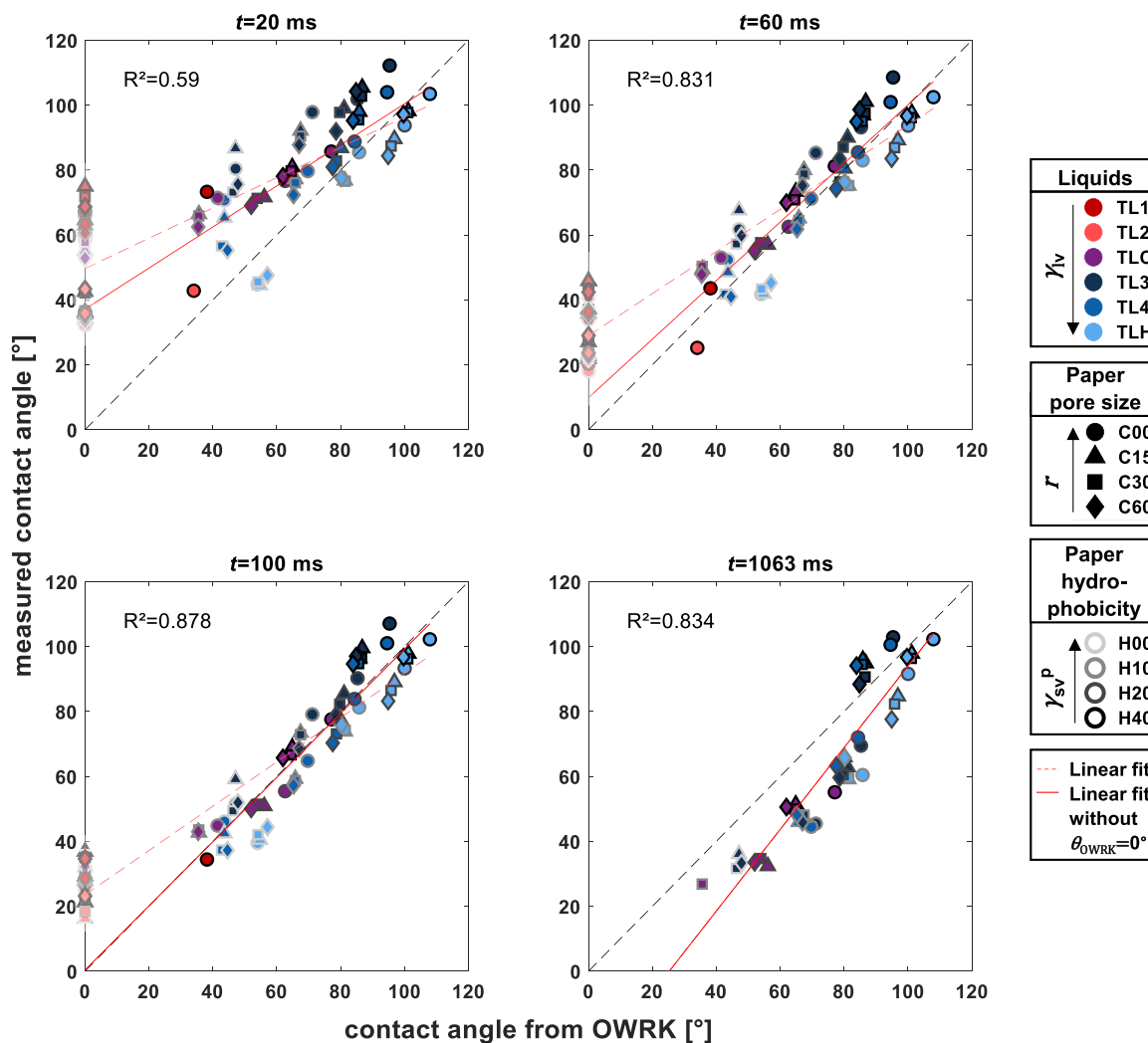
Fig. 8. Comparison of contact angles calculated using the OWRK approach (Eq. (5)) vs. measured contact angles at different evaluation times. Liquids are represented by marker color, substrate pore size by marker shape and substrate hydrophobicity by marker edge color. Data points with a predicted contact angle of 0° are depicted in a paler color as 0° cannot be measured. Excluding OWRK contact angles of 0°, predicted and measured contact angles are equally high after 100 ms and can be predicted with a high R^2 of 0.88. R^2 values correspond to linear fits excluding OWRK contact angles of 0° (red solid line). A linear fit including all data points is represented by a red dashed line. (For interpretation of the references to color in this figure legend, the reader is referred to the web version of this article.)

Since drop absorption speeds could not be determined for all substrate-liquid pairings, it is of further interest if the LW-OWRK model can successfully predict liquid penetration speed also in strong wetting situations. Fig. 10 (a) shows the results of the ultrasonic liquid penetration measurements compared to the penetration speeds predicted with the LW-OWRK model. With $R^2 = 0.895$ an even higher value than for the drop absorption results is reached. Again, the evaluation is dominated by extreme values and it is therefore more useful to rely on a log–log plot (Fig. 10 (b)). In the logarithmic diagram, again a high R^2 of 0.87 can be obtained. Thus, it can be concluded that the LW-OWRK model successfully predicts the penetration speeds of 96 substrate-liquid pairings in a wide range of penetration speeds, also including strong wetting situations. Furthermore, the results of the combined LW-OWRK model can be compared to the LW-equation using measured contact angles instead of the OWRK approach (result diagrams can be found in Figure S7 of the ESI). Interestingly, the predictive power of the combined LW-OWRK model is even slightly better than if measured contact angles are used.

Please note that the penetration speed dh/dt decreases linearly with penetration depth h, which can immediately be seen in Eq. (1). The absolute value of the penetration speed thus depends considerably on the chosen penetration depth. The penetration speeds of the two methods were measured at similar penetration depths (for a detailed discussion please refer to section 5.2 of the ESI). For the calculation, a constant penetration depth of 50 μm – i.e. about half the sheet thickness – was assumed. Having a closer look at Fig. 9 one can see that the calculated values predict much faster penetration speeds than measured. This is probably related to the fact that the LW equation assumes a uniform penetration front in cylindric pores, while there is a number of pore sizes and pore geometries in a paper sheet which results in a ragged liquid front and slower penetration. Therefore, the power of the combined LW-OWRK model is not in predicting absolute penetration speeds, but in its capability in predicting trends and correlations. The benefit of the combined approach is that it facilitates analysis how changes in polar and dispersive surface energy are affecting liquid penetration speed, independently for substrate and liquid properties.
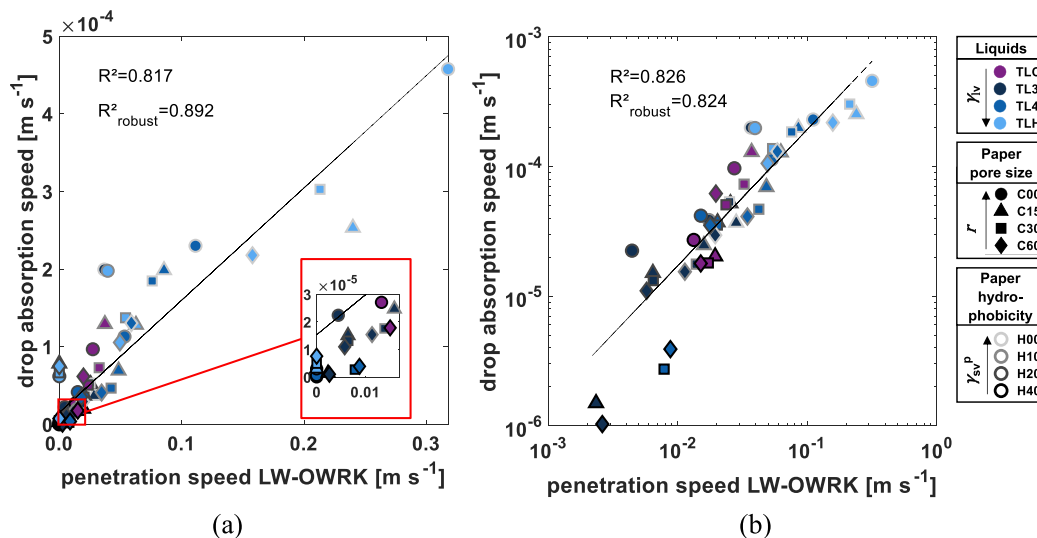
Fig. 9. (a) Penetration speed modelled with the combined LW-OWRK model for a penetration depth of 50 μm versus measured drop absorption speeds. (b) Predicted versus measured data in a log–log chart. Liquids are represented by marker color, paper pore size by marker shape and paper hydrophobicity by marker edge gray level. Data points with strong wetting cannot be captured reliably with this measurement and are excluded. Drop absorption speeds can be predicted well both in the logarithmic and the non-logarithmic diagram.
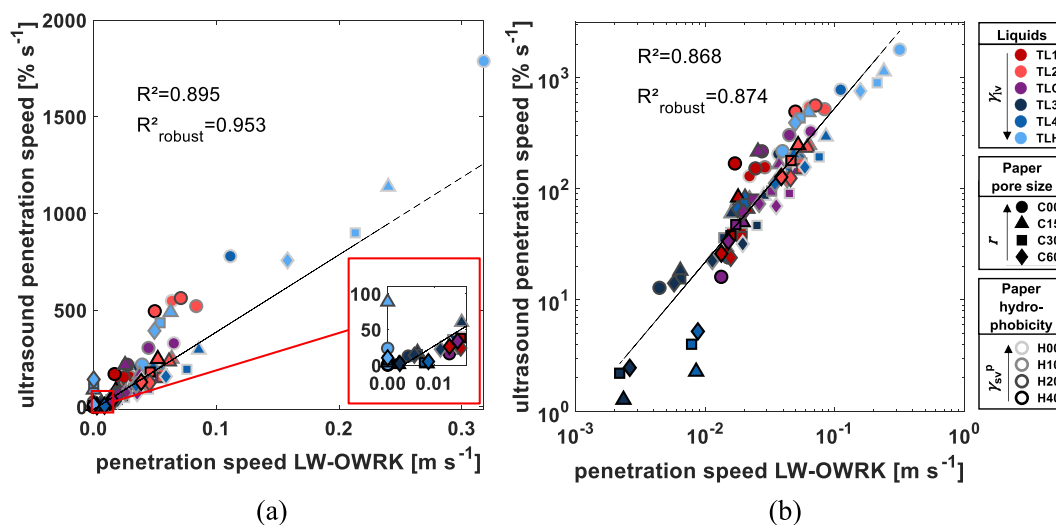
Fig. 10. (a) Penetration speed modelled with the combined LW-OWRK model for a penetration depth of 50 μm versus ultrasonic liquid penetration measurements. (b) Predicted versus measured data in a log–log chart. Liquids are represented by marker color, paper pore size by marker shape and paper hydrophobicity by marker edge gray level. Ultrasonic liquid penetration data can be predicted to a large extent both in the logarithmic and non-logarithmic diagram.

3.2. Performance of LW-Wu and LW-vOGC models

As discussed in the introduction, the contact angle in the Lucas-Washburn equation can also be calculated using other surface energy theories. The results for the combined LW-Wu model (Eq. (9)) and for the LW-vOGC model (Eq. (12)) are reported in section 6.2 and 6.3 of the ESI. Overall, the LW-Wu model also performed rather well, even though the R^2 was a bit lower than for the LW-OWRK model (R^2_{robust} = 0.73 for drop absorption and R^2_{robust} = 0.75 for ultrasound measurements). The LW-vOGC could only be evaluated for the water measurements with the available data. Water penetration speeds were predicted very well for both ultrasound (R^2_{robust} = 0.96) and drop absorption (R^2_{robust} = 0.92) measurements. These results are similar to the results of the LW-OWRK model for water (also shown in the ESI).

3.3. Application case: Tuning substrates with the LW-OWRK model using database liquid data

Any of the combined models can be readily applied using database data existing for many liquids and surfaces. Water penetration speeds measured in this work could be predicted similarly well using a range of literature values for the surface tension components of water (detailed results can be found in section 6.4 of the ESI). The results prove that literature values can be used together with the combined models. This data can then be used for simulations which can help to determine how either substrate or liquid properties need to be optimized in order to achieve a desired penetration behavior. In section 6.4 of the electronic supplementary information (ESI), we discuss an application case for which the substrate surface energy needs to be optimized to achieve a desired water penetration behavior. The problem can be addressed

by drawing a design diagram using the LW-OWRK model which shows the effect of changing the substrate surface energy components on the water penetration speed and then choosing a substrate material showing the desired liquid penetration behavior.

4. Conclusions

The Lucas-Washburn equation [1,2] has been used for about a century to describe capillary liquid penetration. Numerous modifications have been proposed since, e.g. [3–8], for a comprehensive review compare [9]. However, all these models use the contact angle to describe liquid–solid interaction. This has a major drawback: The contact angle is depending on both, liquid and solid. For modeling and engineering optimizations of the liquid penetration in porous materials it would be desirable to predict the penetration speed directly from liquid and solid properties. In a first step Lavi and Marmur [22] tried to estimate a maximum possible liquid penetration speed using OWRK substrate and liquid surface energies.

In this work we have proposed a modelling approach with independent properties of the substrate (pore size, surface energy components) and the liquid (viscosity, surface tension, surface tension components), utilizing either OWRK, Wu or vOGC theory to replace the contact angle in the LW-equation. Comprehensive validation of these three models has been performed. Liquid penetration was measured for a systematic combination of 96 paper-liquid pairings using two measurement methods – drop absorption and ultrasound. The results of both measurements were successfully predicted by the proposed LW-OWRK model ($R^2 = 0.82$–0.90) and to a bit lesser extent with the combined LW-Wu model ($R^2_{robust} = 0.73$–0.75). With the combined LW-vOGC model, water penetration speeds could be predicted similarly well as with the combined LW-OWRK model ($R^2 = 0.93$). We have also presented an application example, how a set of optimal solid–liquid combinations can be found for a predefined liquid penetration behavior, using the proposed model.

We believe that combining the Darcy / LW equation with surface energy theories is very useful for modeling- or engineering applications where liquid absorption in porous media is to be predicted or tuned. The key advantage of the proposed approach is that no measurement of the liquid–solid interaction (contact angle) is required any more. Instead, the model is entirely working with physical data of the solid and the liquid phase, which can be retrieved from databases or measured as described. In our opinion this is opening the potential for all applications where liquid absorption into porous media is relevant, like e.g. soil engineering, bio-composites, microfluidics, construction materials, filters, membranes, barrier materials, paper and textiles.

CRediT authorship contribution statement

Carina Waldner: Conceptualization, Data curation, Formal analysis, Investigation, Methodology, Software, Validation, Visualization, Writing – original draft, Writing – review & editing. **Ulrich Hirn:** Conceptualization, Funding acquisition, Methodology, Supervision, Validation, Writing – original draft, Writing – review & editing.

Data availability

Data will be made available on request.

Declaration of Competing Interest

The authors declare that they have no known competing financial interests or personal relationships that could have appeared to influence the work reported in this paper.

Appendix A. Supplementary data

Supplementary data to this article can be found online at https://doi.org/10.1016/j.jcis.2023.02.116.

References

[1] R. Lucas, Über das Zeitgesetz des kapillaren Aufstiegs von Flüssigkeiten, Kolloid-Zeitschrift. 23 (1918) 15–22.
[2] E.W. Washburn, The dynamics of capillary flow, Phys. Rev. 17 (1921) 273–283.
[3] D. Benavente, P. Lock, M. Ángeles García Del Cura, S. Ordóñez, Predicting the capillary imbibition of porous rocks from microstructure, Transp. Porous Media. 49 (2002) 59–76, https://doi.org/10.1023/A:1016047122877.
[4] R.R. Rye, J.A. Mann, F.G. Yost, The flow of liquids in surface grooves, Langmuir. 12 (1996) 555–565, https://doi.org/10.1021/la9500989.
[5] J.C. Cai, B.M. Yu, M.F. Mei, L. Luo, Capillary rise in a single tortuous capillary, Chinese Phys. Lett. 27 (2010) 1–4, https://doi.org/10.1088/0256-307X/27/5/054701.
[6] A. Shen, Y. Xu, Y. Liu, B. Cai, S. Liang, F. Wang, A model for capillary rise in micro-tube restrained by a sticky layer, Results Phys. 9 (2018) 86–90, https://doi.org/10.1016/j.rinp.2018.02.026.
[7] D. Schebarchov, S.C. Hendy, Dynamics of capillary absorption of droplets by carbon nanotubes, Phys. Rev. E - Stat. Nonlinear, Soft Matter Phys. 78 (2008) 1–6, https://doi.org/10.1103/PhysRevE.78.046309.
[8] D. Feng, X. Li, X. Wang, J. Li, T. Zhang, Z. Sun, M. He, Q. Liu, J. Qin, S. Han, Capillary filling of confined water in nanopores: Coupling the increased viscosity and slippage, Chem. Eng. Sci. 186 (2018) 228–239, https://doi.org/10.1016/j.ces.2018.04.055.
[9] J. Cai, T. Jin, J. Kou, S. Zou, J. Xiao, Q. Meng, Lucas-Washburn equation-based modeling of capillary-driven flow in porous systems, Langmuir. 37 (2021) 1623–1636, https://doi.org/10.1021/acs.langmuir.0c03134.
[10] S. Krainer, U. Hirn, Contact angle measurement on porous substrates: Effect of liquid absorption and drop size, Colloids Surfaces A Physicochem. Eng. Asp. 619 (2021) 126503, https://doi.org/10.1016/j.colsurfa.2021.126503.
[11] T. Young, An essay on the cohesion of fluids, Philos. Trans. R. Soc. 95 (1805) 65–87.
[12] D.K. Owens, R.C. Wendt, Estimation of the surface free energy of polymers, J. Appl. Polym. Sci. 13 (1969) 1741–1747.
[13] D.H. Kaelble, Dispersion-polar surface tension properties of organic solids, J. Adhes. 2 (1970) 66–81, https://doi.org/10.1080/00218467008544582.
[14] W. Rabel, Einige Aspekte der Benetzungstheorie und ihre Anwendung auf die Untersuchung und Veränderung der Oberflächeneigenschaften von Polymeren, Farbe Und Lack. 77 (1971).
[15] C.J. van Oss, R.J. Good, M.K. Chaudhury, Additive and nonadditive surface tension components and the interpretation of contact angles, Langmuir. 4 (1988) 884–891, https://doi.org/10.1021/la00082a018.
[16] S. Wu, Polar and nonpolar interactions in adhesion, J. Adhes. 5 (1973) 39–55, https://doi.org/10.1080/00218467308078437.
[17] A.W. Neumann, R.J. Good, C.J. Hope, M. Sejpal, An equation-of-state approach to determine surface tensions of low-energy solids from contact angles, J. Colloid Interface Sci. 49 (1974) 291–304, https://doi.org/10.1016/0021-9797(74)90365-8.
[18] D. Li, A.W. Neumann, Equation of state for interfacial tensions of solid-liquid systems, Adv. Colloid Interface Sci. 39 (1992) 299–345, https://doi.org/10.1016/0001-8686(92)80064-5.
[19] S. Ahadian, M. Mohseni, S. Moradian, Ranking proposed models for attaining surface free energy of powders using contact angle measurements, Int. J. Adhes. Adhes. 29 (2009) 458–469, https://doi.org/10.1016/j.ijadhadh.2008.09.004.
[20] V. Gurau, M.J. Bluemle, E.S. De Castro, Y.M. Tsou, J.A. Mann, T.A. Zawodzinski, Characterization of transport properties in gas diffusion layers for proton exchange membrane fuel cells. 1. Wettability (internal contact angle to water and surface energy of GDL fibers), J. Power Sources. 160 (2006) 1156–1162, https://doi.org/10.1016/j.jpowsour.2006.03.016.

[21] V. Gurau, J.A. Mann, Technique for characterization of the wettability properties of gas diffusion media for proton exchange membrane fuel cells, J. Colloid Interface Sci. 350 (2010) 577–580, https://doi.org/10.1016/j.jcis.2010.07.011.

[22] B. Lavi, A. Marmur, The capillary race: Optimal surface tensions for fastest penetration, Colloids Surfaces A Physicochem. Eng. Asp. 282–283 (2006) 263–271, https://doi.org/10.1016/j.colsurfa.2006.01.033.

[23] S. Krainer, C. Smit, U. Hirn, The effect of viscosity and surface tension on inkjet printed picoliter dots, RSC Adv. 9 (2019) 31708–31719, https://doi.org/10.1039/c9ra04993b.

[24] ASCE Library , Density and viscosity of water 0 °C - 40 °C (2006). https://doi.org/10.1061/9780784408230.ap02.

[25] B. Janczuk, W. Wojcik, A. Zdziennicka, Determination of the components of the surface tension of some liquids from interfacial liquid-liquid tension measurements, J. Colloid Interface Sci. 157 (1993) 384–393.

[26] J.D. Berry, M.J. Neeson, R.R. Dagastine, D.Y.C. Chan, R.F. Tabor, Measurement of surface and interfacial tension using pendant drop tensiometry, J. Colloid Interface Sci. 454 (2015) 226–237, https://doi.org/10.1016/j.jcis.2015.05.012.

[27] C. Waldner, A. Mayrhofer, U. Hirn, Measuring liquid penetration in thin, porous sheets with ultrasound and drop absorption – scope and limitations, Colloids Surfaces A Physicochem. Eng. Asp. 650 (2022) 129551, https://doi.org/10.1016/j.colsurfa.2022.129551.

[28] C. Waldner, U. Hirn, Ultrasonic liquid penetration measurement in thin sheets – physical mechanisms and interpretation, Materials (Basel). 13 (2020) 2754, https://doi.org/10.3390/ma13122754.

[29] D.Y. Kwok, A.W.U. Neumann, Contact angle measurement & contact angle interpretation, Adv. Colloid Interface Sci. 81 (1999) 167–249, https://doi.org/10.1016/S0001-8686(98)00087-6.

[30] R.J. Good, Contact angle, wetting, and adhesion: a critical review, J. Adhes. Sci. Technol. 6 (1992) 1269–1302.

[31] Z. Zhang, W. Wang, A.N. Korpacz, C.R. Dufour, Z.J. Weiland, C.R. Lambert, M.T. Timko, Binary liquid mixture contact-angle measurements for precise estimation of surface free energy, Langmuir. 35 (2019) 12317–12325, https://doi.org/10.1021/acs.langmuir.9b01252.

[32] O. Myronyuk, D. Baklan, L. Nudchenko, Evaluation of the surface energy of dispersed aluminium oxide using Owens-Wendt theory, Technol. Audit Prod. Reserv. 2 (2020) 25–27, https://doi.org/10.15587/2312-8372.2020.200756.

[33] K.Y. Law, H. Zhao, Surface wetting: Characterization, contact angle, and fundamentals, Springer Cham (2015), https://doi.org/10.1007/978-3-319-25214-8.